

Strong Plasmon–Exciton Interactions on Nanoantenna Array–Monolayer WS₂ Hybrid System

Lin Liu, Landobasa Y. M. Tobing, Xuechao Yu, Jinchao Tong, Bo Qiang, Antonio I. Fernández-Domínguez, Francisco J. Garcia-Vidal, Dao Hua Zhang,* Qi Jie Wang,* and Yu Luo*

Strong plasmon–exciton interactions in monolayer transition-metal dichalcogenides (TMDs) is emerging as a promising material platform for light emissions, nonlinear optics, and quantum communications, and their realizations require highly localized electric fields parallel to the transition dipole moment of TMD excitons. Here, a systematic study of light–matter interaction in planar dimer nanoantenna of nanoscale gaps coupled with monolayer WS₂ is presented, where the effects of the local field enhancement and spatial mode overlap in the plasmon–exciton coupling strength are experimentally investigated. Importantly, anticrossing behaviors in the strong coupling regime with a Rabi splitting of $\Omega = 118$ meV for gold bowtie antennas with 7 nm gaps and $\Omega = 138$ meV for gold dimer arrays with 10 nm gaps are demonstrated.

1. Introduction

The interaction of highly localized modes with nanoscale emitters has gained much attention in the past decades^[1–3] for its importance in fundamental quantum physics, such as Bose–Einstein condensation,^[4–7] quantum vortex^[8] and non-Hermitian physics^[9,10] and applications in optical transistors,^[11,12] polariton switches^[13,14] and single photon sources.^[15] Based on the energy exchange rate between matter and electromagnetic modes relative to their respective damping constants, light–matter interaction strength can be classified into weak and strong coupling regimes. In a weakly-coupled system, optical processes involving light and matter are irreversible,


exemplified in spontaneous emissions of quantum emitters.^[16–19] However, this is qualitatively different when the light–matter interaction enters the strong coupling regime, where coherent oscillations of energy between excitons and photons dominates over the electromagnetic damping, manifesting in clear spectral splitting known as the Rabi splitting.^[20–23] Realization of strong coupling requires a large density of photonic states, which is mainly dependent on the spatiotemporal confinement of electromagnetic fields characterized by the mode volume V and resonance Q -factor, $LDOS \propto Q/V$.

For this, many efforts have been devoted

to realize photonic microcavities with high Q/V , namely, high finesse resonators based on photonic crystals^[24–26] and whispering gallery modes.^[27] Despite their ultrahigh Q resonances, realizations of strong coupling in these platforms often require their characterizations implemented in cryogenic temperatures due to the mismatch between the photon and exciton lifetimes. In addition, light–matter coupling occurs within an interaction volume dictated by the diffraction-limit, thereby hindering the characterization of light–matter interaction at a single molecule level. Alternatively, plasmonic systems have been explored for strong light–matter interaction at the nanoscale, particularly because plasmonic nanocavities also exhibit high Q/V due to their strong field confinement at the deep subwavelength scale despite their much lower Q -factor than their dielectric counterparts. Different kinds of quantum emitters have been explored for studying strong coupling with plasmonic nanostructures, including J-aggregates,^[28–32] dye molecules^[33–35] and quantum dots.^[36,37] Recently, monolayers made of transition metal dichalcogenides (TMDs), when combined with plasmonic nanostructures, have been shown to be excellent platforms for achieving strong coupling at room temperature due to their direct bandgap and strong binding energy of their excitons.^[38,39]

Different kinds of plasmonic systems have been explored for plasmon–exciton coupling with TMDs, including nanocavities,^[40] self-assembled metallic nanoparticles,^[41–44] nanoantenna arrays,^[17,45–47] and metal nanohole arrays.^[48] For strong coupling, it is important to design plasmonic nanocavities with a mode field parallel to the transition dipole moment of the excitons in TMDs. In nanoparticle on mirror (NPoM) systems,^[40] for example, multilayered TMDs are used such that

L. Liu, Dr. L. Y. M. Tobing, Dr. X. Yu, Dr. J. Tong, Dr. B. Qiang, Prof. D. H. Zhang, Prof. Q. J. Wang, Prof. Y. Luo
School of Electrical & Electronic Engineering
Nanyang Technological University
Singapore 639798, Singapore
E-mail: edhzhang@ntu.edu.sg; qjwang@ntu.edu.sg; luoyu@ntu.edu.sg
Prof. A. I. Fernández-Domínguez, Prof. F. J. Garcia-Vidal
Departamento de Física Teórica de la Materia Condensada and
Condensed Matter Physics Center (IFIMAC)
Universidad Autónoma de Madrid
28049 Madrid, Spain
Prof. F. J. Garcia-Vidal
Donostia International Physics Center (DIPC)
20018 Donostia-San Sebastian, Spain

 The ORCID identification number(s) for the author(s) of this article can be found under <https://doi.org/10.1002/adom.201901002>.

DOI: 10.1002/adom.201901002

the transition dipole moment of the TMDs is reoriented toward the out-of-plane resonance mode field. However, for monolayer TMD in which the transition dipole moment is purely in-plane, the plasmonic mode of the NPoM system only couples weakly to the exciton despite its strong field enhancement in the dielectric spacer separating the nanoparticle and the metal film, which is largely due to its orthogonal mode field. In the context of synthesized nanoparticles, attempts to reduce misalignment between the mode field and the exciton transition dipole have been explored, notably in the use of gold bi-pyramids^[43] and ultrathin gold nanodisks.^[44]

Meanwhile, top-down fabricated planar nanoantennae with nanogaps exhibit strong in-plane mode fields, and have been demonstrated to couple strongly with quantum emitters.^[49–51] The main advantage of the top-down fabricated antennae lies in their lithographic flexibility, which could be used as a platform for studying light–matter interaction with TMD, for example in the moderate coupling of bowtie nanoantenna with monolayer MoS₂ that manifests in the emergence of Fano resonances.^[17] In this work, we present an in-depth analysis of the strong-coupling anticrossing characteristics in planar gold nanoantenna with nanogaps, namely bowtie and square dimer nanoantennae. By fabricating nanoantennae of different gaps, sizes, and periodicity on the same chip, we are able to investigate systematically the roles of *E*-field enhancements and spatial mode overlap in the coupling strength. By introducing ultrathin dielectric interlayer, we observe the effect of spatial mode overlap where ≈20–30% decrease of Rabi splitting is observed when 2 nm thick Al₂O₃ layer is inserted. Specifically, we experimentally demonstrate a direct evidence for the correlation between the local density of states and the coupling strength. We demonstrate a Rabi splitting of Ω = 138 meV based on square dimer of sub-10 nm gaps, which is shown to be in strong-coupling regime and confirmed by photoluminescence measurements of TMD-dimer systems based on CVD-grown and exfoliated monolayer WS₂.

2. Theoretical Model

The strong coupling of a plasmonic resonance with excitons supported by a monolayer TMD can be understood from the so-called Jaynes–Cummings (JC) Hamiltonian, which describes the interaction of electromagnetic field with a two-level atom^[52,53]

$$\hat{H}_{\text{JC}} = \omega_{\text{pl}} \hat{a}^\dagger \hat{a} + \omega_0 \hat{\sigma}_z / 2 + g_c (\hat{a} \hat{\sigma}_+ + \hat{a}^\dagger \hat{\sigma}_-) \quad (1)$$

where the first term describes the electromagnetic energy characterized by the plasmon mode frequency ω_{pl} , the second term describes the two-level excitation characterized by exciton frequency ω_0 , and the third term describes the exciton-photon interaction characterized by coupling strength g_c . \hat{a}^\dagger and \hat{a} is the creation and annihilation operators for the photon, while $\hat{\sigma}_+$ and $\hat{\sigma}_-$ are the raising and lowering operators for the exciton. $\hat{\sigma}_z$ is the atomic inversion operator. Rearranging the JC Hamiltonian into an eigenvalue problem for the hybrid states gives

$$\begin{pmatrix} \omega_{\text{pl}} + i\gamma_{\text{pl}}/2 & g_c \\ g_c & \omega_0 + i\gamma_0/2 \end{pmatrix} \begin{pmatrix} \alpha \\ \beta \end{pmatrix} = \omega_{\pm} \begin{pmatrix} \alpha \\ \beta \end{pmatrix} \quad (2)$$

where (α, β) are eigen coefficients satisfying $|\alpha|^2 + |\beta|^2 = 1$, and

$$\omega_{\pm} = \frac{1}{2} \left(\omega_{\text{pl}} + \omega_0 + i \frac{\gamma_{\text{pl}} - \gamma_0}{2} \right) \pm \frac{1}{2} \sqrt{\left(\omega_{\text{pl}} - \omega_0 + i \frac{\gamma_{\text{pl}} - \gamma_0}{2} \right)^2 + 4g_c^2} \quad (3)$$

are the eigenfrequencies ω_{\pm} of the hybrid modes, with γ_{pl} and γ_0 as the dissipation rates of uncoupled plasmon and exciton modes. By ignoring the dissipation terms, the eigenfrequencies can be simplified as^[54,55]

$$\omega_{\pm} = \frac{1}{2} (\omega_{\text{pl}} + \omega_0) \pm \sqrt{g_c^2 + \delta^2 / 4} \quad (4)$$

with $\delta = \omega_{\text{pl}} - \omega_0$ as the detuning between plasmon mode and exciton energy. The vacuum Rabi splitting is the resonance splitting at zero detuning, $\Omega = 2g_c$, which can be derived from Equation (4) at zero detuning as $\Omega = \sqrt{(\omega_{\text{pl}} - \omega_0)(\omega_0 - \omega_{\text{pl}})}$. The system is said to be in strong coupling when the rate of energy exchange is faster than the loss. The rather generic criterion for strong coupling is $\Omega > (\gamma_+ + \gamma_-)/2$, where γ_{\pm} are the linewidth of the split polaritonic modes. A more rigorous criterion for the strong coupling has been studied in detail,^[56] suggesting that strong coupling is achieved when $|\Omega/(\gamma_{\text{pl}} - \gamma_0)| > 1$. For *N* excitons coupled with a plasmon mode, the coupling strength can be written as: $g_c = \sqrt{N} \mu_e |E_{\text{pl}}|$, where μ_e is the transition dipole moment of exciton and $|E_{\text{pl}}| = \sqrt{\hbar\omega/2\epsilon\epsilon_0 V}$ is the plasmonic field. The quality factor of the plasmonic antenna can be calculated as $Q = \omega_{\text{pl}}/\gamma_{\text{pl}}$. Therefore, strong plasmon–exciton coupling is related with LDOS as $g_c^2/\gamma_{\text{pl}} \approx Q(N/V)$.

3. Results and Discussions

As shown in **Figure 1**, we present a detailed study of plasmon–exciton coupling of gold nanoantenna arrays lithographically fabricated on monolayer WS₂ films deposited on SiO₂/Si substrates, where square dimer and bowtie antenna designs were chosen in this study for their strong local *E*-fields across nanogaps and their small mode volume. As commented above, the advantage of these top-down fabricated antennae over self-assembled nanoparticle on mirror (NPoM) systems lies in their in-plane local *E*-fields that align with the transition dipole moment of the monolayer WS₂. Furthermore, the lithographic flexibility of the top-down fabrication allows us to tune the antenna dimensions for studying plasmon–exciton coupling at different resonance detuning. We also introduced an ultrathin dielectric spacer between the WS₂ and gold nanoantenna for investigating the effect of the plasmon mode spatial overlap with the WS₂ to the plasmon–exciton coupling strength. The scanning electron micrographs (SEMs) of the fabricated gold nanostructures are shown in Figure 1c (bowtie nanoantenna) and Figure 1d (square dimer). In order to ensure a small mode volume, we fabricated these nanoantenna with gap spacing (*g*) in ≈10 nm range (see the Experimental Section). The other parameters such as the side length (*s*) and apex angle (θ) were chosen to match the plasmon mode frequency (ω_{pl}) close to the WS₂ exciton transition (ω_0). The periodicities (P_x, P_y) of the nanoantenna array were designed as $P_x = P_y = 4s$ to minimize

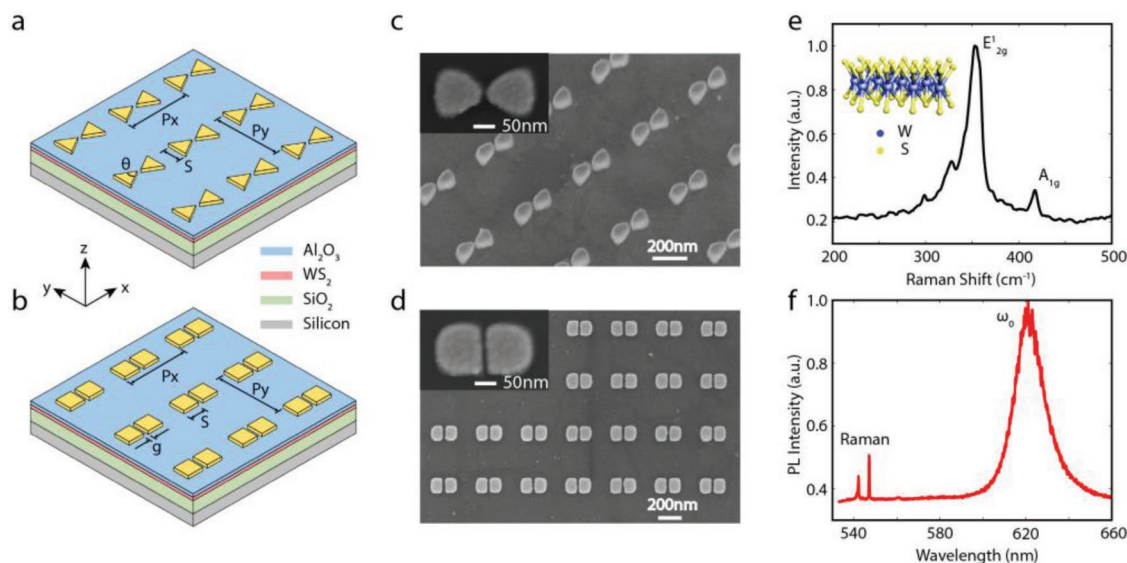


Figure 1. Hybrid TMDC-nanoantenna array systems. a,b) Schematics of gold bowtie and square dimer arrays coupled with monolayer WS₂ separated by dielectric spacer layer. c,d) Scanning electron microscopy images of the fabricated gold nanoantenna with sub-10 nm gaps. e) Raman spectrum and f) photoluminescence of monolayer WS₂.

the near-field coupling between nanoantennae, which is known to impart resonance broadening and, consequently, decreases the Q factor. This is confirmed in our numerical simulations which reveals that the scattering cross sections (σ_{scat}) of the nanoantenna are smaller than the unit cell area ($\sigma_{\text{scat}} < P_x P_y$). However, the far-field coupling still exists among these nanoantenna due to the strong radiation of the dimer antenna. We used this far-field coupling to further enhance the local E -fields, from which our numerical simulation show that the E -field can be $\approx 2.5\times$ higher in a nanoantenna array (with $P_{x,y} = 4s$) than in an isolated antenna. Another purpose of using the nanoantenna array is to investigate the mode interaction under two mode excitations. The first type is the normal excitation (in bright field geometry), which generates a Fano-like resonance that results from the interaction between the localized surface plasmon (LSP) of the gold nanoantenna and the thin film resonance of the 295 nm thick SiO₂ film. The second type is the oblique excitation (in dark field geometry) which generates only the LSP modes.

The WS₂ considered in this work was grown by chemical vapor deposition (CVD) instead of realized by mechanical exfoliation. Despite the lower optical quality of the former, we note the importance of the large-scale uniformity of the WS₂ film in this study, particularly in the context of characterizing plasmon–exciton couplings with gold nanoantenna arrays fabricated across the sample. For transition metal dichalcogenide (MX₂) layered compounds (M = Mo, W and X = S, Se, Te), there are generally four Raman-active modes, namely the A_{1g}, E_{1g}, E_{2g}¹ and E_{2g}² modes.^[57] In order to investigate the monolayer properties of the CVD-grown WS₂, we focus our attention to the in-plane vibrational E_{2g}¹ mode and the out-of-plane vibrational A_{1g} mode, where the former shows little dependence on the film thickness and the latter undergoes a blue shift with increasing layer number.^[58] As shown in Figure 1e, Raman characterization of the CVD-grown WS₂ shows the E_{2g}¹ mode at 353 cm⁻¹

and A_{1g} mode 417 cm⁻¹ with a 64.1 cm⁻¹ frequency difference between the two modes. This value is close to the 65.5 cm⁻¹ frequency difference for monolayer WS₂ in other report,^[58] thereby confirming the monolayer characteristics of our CVD-grown WS₂. The photoluminescence of our CVD-grown WS₂ (under 532 nm laser excitation) is presented in Figure 1f, showing exciton peak at $\omega_0 = 2$ eV with $\gamma_0 = 25$ meV linewidth. We also note the two small peaks near the 532 nm excitation, which are the two Raman signals in Figure 1e.

The mappings of the optical response of the gold nanoantenna arrays were carried out by hyperspectral imaging system (see the Experimental Section) schematically illustrated in the Supporting Information (Figure S1). Figure 2a displays the x -polarized scattering spectrum (in the bright-field geometry) of square dimer arrays coupled with monolayer WS₂ with near zero detuning ($s = 60$ nm, $g = 20$ nm), where a weak dip is observed near the exciton transition in between more pronounced resonance dips. The weak dip signifies the mode splitting which results from the plasmon–exciton coupling, with the split modes indicated by the weak scattering peaks. Such an obscured spectral splitting is attributed to the hybrid mode resulting from the interference between the LSP mode of the nanoantenna and the mode arising from the multiple reflections inside the 295 nm SiO₂ film. In order to verify if this is indeed caused by multiple reflection that builds up only under normal incidences, we excite the square dimers under oblique illumination (in the dark-field geometry). As evident in Figure 2b, we observed an optical response with clear mode splitting at the exciton transition (denoted by the shaded band), indicating the absence of the Fabry–Perot (FP)-like mode under oblique excitation. The small bump around 546 nm is not associated with any resonance as it is the spectral artifact of the mercury lamp itself. The hybridization of this mode is numerically simulated in Figure 2c, which shows that the two dips at 500 and 700 nm stem from the modified FP resonance

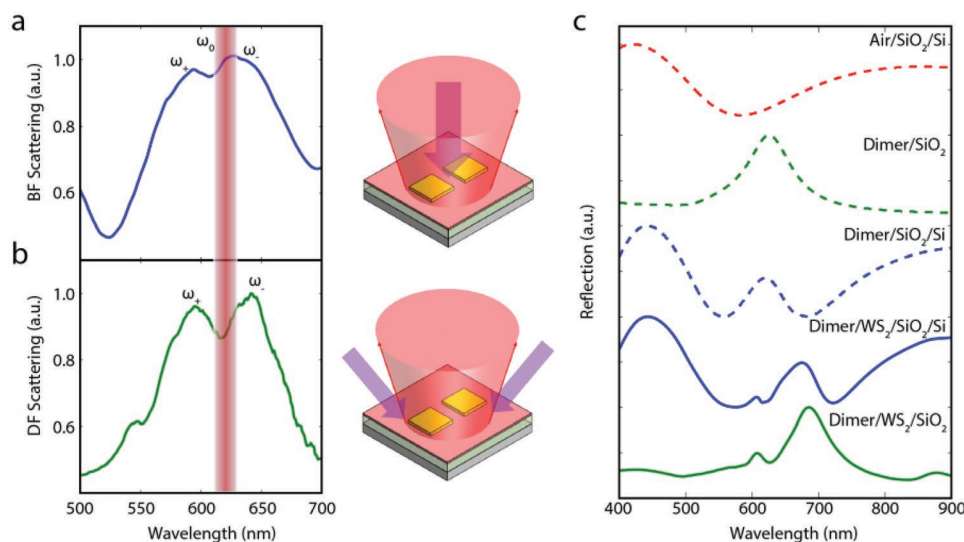


Figure 2. Resonance splitting near zero detuning for gold square dimer coupled with monolayer WS_2 . a) Bright-field and b) dark-field optical responses of square dimers with nominal side length $s = 60$ nm and gap spacing $g = 20$ nm. The optical response of monolayer WS_2 exciton ($\omega_0 = 2$ eV) is denoted by the red band whose width represents the emission linewidth ($\gamma_0 = 64$ meV). c) Fullwave simulations depicting mode interference between LSP resonance of gold nanoantenna and FP resonance of multiple thin film reflections.

condition due to the presence of gold nanoantenna (dashed blue curve). The phase response (ϕ) of a strongly radiating plasmonic antenna such as dimer or disk is close to $\phi = \pi$ at LSP resonance (for negligible damping loss), translating to a rapid change of the FP interference condition from constructive to destructive, satisfying the FP resonance condition in two different frequencies. Thus, in addition to the LSP resonance position that remains unchanged, we observe two reflectance dips associated with light localization inside SiO_2 film. In the presence of monolayer WS_2 , a mode splitting is to be expected for the reflection peak at the exciton transition (solid blue curve). The simulated spectra differ from the measure spectra notably in their spectral contrasts. Such a difference in spectral contrast is attributed to the nonideal mode excitation in our experiment, where the plasmonic nanoantenna arrays were excited at different incident angles dictated by the numerical aperture of our objective lens (which is $\text{NA} = 0.55$). Other factors include the permittivity of both the physically deposited gold and the CVD-grown WS_2 monolayer, and also the surface roughness and roundedness in the gold nanoantenna structure.

We present in **Figure 3** anticrossing behaviors of gold bowtie and square dimer arrays coupled with monolayer WS_2 based on dark-field measurements. The upper (ω_+) and lower (ω_-) energy branches of the hybrid modes are plotted for different resonance detunings ($\delta = \omega_{\text{pl}} - \omega_0$), realized through geometric variations of the nanoantenna. Red dashed line denotes the WS_2 exciton energy at 2 eV, while the blue and green solid curves denote the fitting based on Equation (4). In Figure 3a, we present the anticrossing behavior for gold bowtie nanoantenna, which were fabricated with different nominal apex angles ($\theta = 40^\circ, 50^\circ, 60^\circ$) and side lengths ($s = 60, 80, 100$ nm). Although the gap spacing was nominally fixed as $g = 20$ nm, the actual gap spacing in the fabricated structures can be tuned by adjusting the exposure dose and time. In our experiments, we have realized bowtie antenna with gaps as small as $g \approx 7$ nm with

good repeatability. The Rabi splitting for WS_2 -bowtie system was found to be $\Omega = 118$ meV. In Figure 3b, we present the anticrossing behavior for gold square dimer, which were fabricated with different nominal side lengths ($s = 60, 80, 100$ nm) and gap spacings ($g = 20, 30, 40$ nm). Similar to bowtie structures, the real gap spacings were realized by tuning the exposure dose and develop time, from which gold square dimer with gap as small as $g \approx 10$ nm have been realized. The Rabi splitting for WS_2 -dimer system was found to be $\Omega = 138$ meV. It is worth noting that wider Rabi splitting is observed for the square dimers than for bowtie antennae despite the smaller mode volume of the latter, which indicates the higher Q/V values and therefore larger local density of states (LDOS) of the former. This is verified by the smaller local E -field of the bowtie antenna (Figure 3e), as compared to that of the square dimer (Figure 3f). The geometry shapes of the nanoantenna arrays were designed to have LSP resonances near WS_2 transition at 620 nm (2 eV). The details of geometrical structures, resonance wavelength, Q factor and mode area for the two structures are given in Table S1 (Supporting Information), showing that square dimer antenna exhibits 70% higher Q -factor with 26% larger mode area compared to those of the bowtie antenna. The role of E -field enhancement in the coupling strength is studied in isolated square dimers separated by much larger periodicity ($P_{x,y} = 2 \mu\text{m}$). In such situations, both the near-field and far-field couplings can be ignored, which results in $2.5\times$ smaller E -field enhancements for the isolated square dimers (Figure S3c,d, Supporting Information). The much higher field enhancement in nanoantenna arrays is attributed to Rayleigh–Wood anomaly arising from the diffraction condition of the pattern. Periodic patterning of dimers into an array reduces the linewidth of the dimers LSP resonance.^[60,61] The anticrossing behavior for isolated square dimers is given in the Supporting Information (Figure S3b), showing narrower Rabi splitting ($\Omega = 114$ meV) compared to that of the square dimer arrays ($\Omega = 138$ meV).

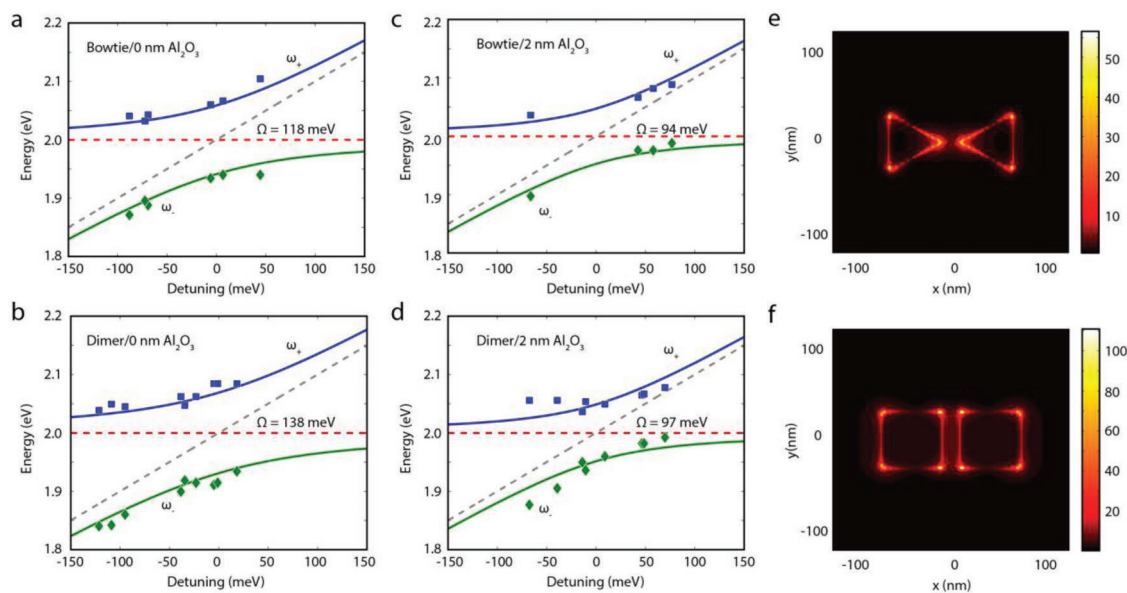


Figure 3. Anticrossing behaviors in strongly coupled systems for a) bowtie and b) square dimer antennae. The effect of 2 nm thick Al₂O₃ spacer in reducing spatial mode overlap is demonstrated for c) bowtie and d) square dimer. Corresponding $|E|^2$ -field distributions at near zero detuning for e) bowtie ($s = 60$ nm, $\theta = 60^\circ$) and f) square dimer ($s = 60$ nm, $g = 20$ nm) arrays.

We have also investigated the role of spatial overlap between the plasmon mode and the excitons in the coupling strength, where an ultrathin dielectric spacer is introduced between the gold nanoantenna array and monolayer WS₂. Insertion of 2 nm thick Al₂O₃ layer leads to a decrease of the Rabi splitting from $\Omega = 118$ to 94 meV for the bowtie antenna (Figure 3c), and from $\Omega = 138$ to 97 meV for the square dimers (Figure 3d). In addition to the decrease of spatial overlap and more light localization within the ultrathin film (Figure S4, Supporting Information), a decrease in the coupling strength is also caused by the increased proportion of the out-of-plane E -fields which does not couple with the in-plane transition dipole moment of the monolayer WS₂ excitons. The strong coupling regimes of our results are evaluated by the two criteria described briefly in the previous section. Using the square dimer represents the largest Rabi splitting in this work, where $\gamma_+ = 70.6$ meV, $\gamma_- = 67.5$ meV, $\gamma_0 = 64$ meV, $\gamma_{pl} = 247.8$ meV, $\Omega = 138$ meV, we found that $\Omega - (\gamma_+ + \gamma_-)/2 \cong 68.9$ meV and $|\Omega/(\gamma_{pl} - \gamma_0)| \cong 1.5$, indicating that our system satisfies strong coupling condition. In the presence of 2 nm Al₂O₃ film, where $\gamma_+ = 65.7$ meV, $\gamma_- = 57.9$ meV, $\Omega = 97$ meV, we found that $\Omega - (\gamma_+ + \gamma_-)/2 \cong 27.95$ meV and $|\Omega/(\gamma_{pl} - \gamma_0)| \cong 1.05$. This suggests that our system is still in strong coupling region, albeit close to the boundary between weak and strong coupling.

Other fingerprints of the plasmon–exciton interaction can be found in the photoluminescence (PL) response of the monolayer WS₂ coupled with square dimers of $s = 80$ nm (blue) and $s = 100$ nm (green). Although the mode splitting associated with strong coupling can be clearly observed in the dark field scattering results, we observe no splitting in the PL response. However, we observed a red shift in the PL emissions accompanied with an increasing shoulder below 620 nm in the WS₂-dimer system (Figure 4a). To further understand this, we plot the PL contribution from the dimer structure, $PL_{\text{dimer}} = PL_{\text{dimer}} - PL_{\text{WS}_2}$, obtained by subtracting the PL response with that

of the WS₂ film (Figure 4a, red curve). As shown in Figure 4b, we note that the spectral dip in the PL response coincides with that in the dark field spectra, but with upper polariton emission (ω_+) much less pronounced than the lower one (ω_-). We found that the splitting in the PL response is narrower than the dark field scattering counterparts, which appears to be in agreement with other works that investigated PL splitting in J-aggregates coupled to silver nanoprisms.^[62] Our numerical calculations also yield a smaller splitting in the absorption cross section than in the scattering one (Figure S6, Supplementary Information). The more pronounced PL peak in the PL splitting may have been caused by the quality of the monolayer WS₂ and the way it couples with the gold nanoantenna. We investigated this using mechanically exfoliated monolayer WS₂ transferred onto gold nanoantenna array (Figure S5, Supporting Information), and found that the PL response exhibits splitting but with more pronounced higher energy emission, contrary to what we observed in Figure 4a. However, the detailed mechanisms for the more pronounced PL peaks remains unclear as there are still many factors influencing the PL response of a strongly coupled system.^[62,63]

4. Conclusion

Strong plasmon–exciton interaction in monolayer WS₂ coupled with gold nanoantenna arrays have been investigated. Bowtie and square dimer antenna of sub-10 nm gaps are employed in this study for their high Q/V property which stems from their strongly confined E -fields across nanogaps. We coupled the exciton with two different modes excited under bright field and dark field geometries, and characterize anticrossing behavior with Rabi splitting as large as 138 meV for gold square dimer arrays. The role of the E -field enhancement in the coupling strength is

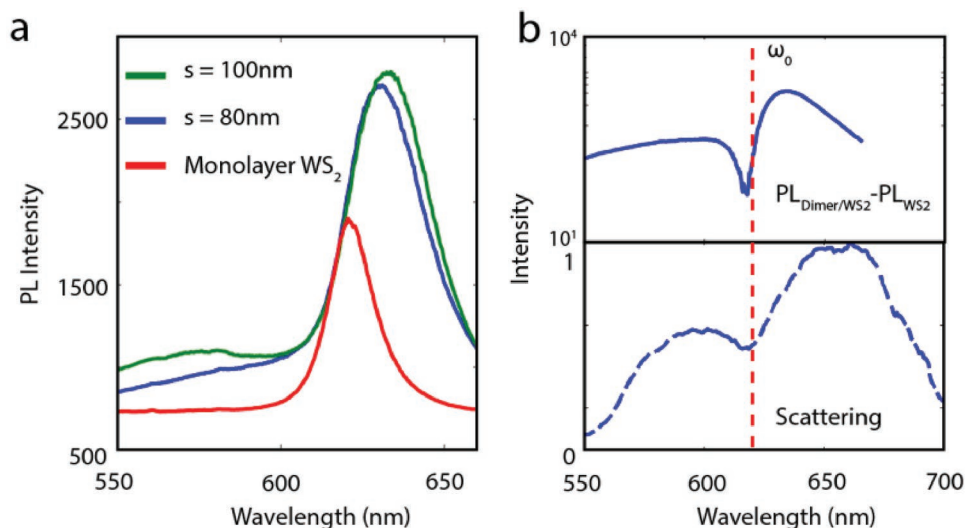


Figure 4. Photoluminescence of WS₂-dimer system. a) PL responses of uncoupled monolayer WS₂ on SiO₂/Si substrate (red curve), and monolayer WS₂ coupled with square dimers with $s = 80$ nm, $g = 30$ nm (blue curve) and $s = 100$ nm, $g = 30$ nm (green curve). b) The PL response of the dimer structure in log-scale, in comparison with the dark fields scattering response of square dimer with $s = 80$ nm, $g = 30$ nm.

studied by eliminating the near-field and far-field couplings in the sparse nanoantenna arrays, which significantly decreases the local E -field, leading to narrower Rabi splitting. The role of the spatial mode overlap is investigated through inserting ultrathin dielectric spacers between nanoantenna and monolayer WS₂, where a 20–30% decrease in the coupling strength is observed when a 2 nm thick Al₂O₃ spacer is introduced. Using the criteria for the strong coupling, the WS₂-dimer system is justified to be in the strong coupling region, even with a 2 nm dielectric spacer. This is mainly attributed to the fact that the in-plane transition dipole of the monolayer WS₂ aligns with the strong in-plane E -fields of the nanoantenna confined within nanoscale gaps. The signature of the strong coupling is also characterized in the PL measurements of our WS₂-dimer system, with a more pronounced lower energy emission. The cause for such asymmetrical PL splitting remains unclear, and future investigations are still needed to understand the PL splitting properties of strongly coupled system.

5. Experimental Section

Sample Fabrication: The full-area WS₂ was grown on 295 nm thick thermal oxide on silicon substrate (from 2DSemiconductors Inc), with the monolayer thickness properties of the WS₂ confirmed by atomic force microscopy (AFM) and Raman spectroscopy. The emission wavelength of the CVD-grown and mechanically exfoliated WS₂ were characterized by micro-photoluminescence. The ultrathin 2 nm thick Al₂O₃ spacer layer for studying the near field coupling between plasmon and WS₂ was deposited by atomic layer deposition (Cambridge Nanotech). The gold dimer and bowtie nanoantenna arrays were fabricated by electron beam lithography (20 keV energy and 30 pA beam current), followed by sonicated cold development in a mixture of n -pentyl acetate and isopropanol at 6 °C temperature; and 30 nm thick gold evaporation at 0.05 nm s⁻¹ rate. The lift-off pattern transfer was then conducted in n -methyl pyrrolidone for 10 min, followed by isopropanol rinse.

Optical Characterization: The samples were characterized in microscope setting coupled to hyperspectral imaging system. In the reflection measurements, mercury lamp (X-Cite 120) was

focused onto the sample via 50× objective lens (NA = 0.55) under bright-field geometry. The signals were directed to the hyperspectral imaging system, while the piezo-controlled stage is scanned in order to obtain the reflection mapping. The reflectance was obtained by normalizing the reflection signals to the reflection of gold film of the same thickness. The scattering measurements followed the same routine but in dark-field geometry. The scattering was normalized to the scattered signals from the substrate. In all these measurements, polarizers were placed after the source and before the hyperspectral imaging system in order to eliminate polarization mixing. The micro-photoluminescence and Raman measurements were conducted by WITec system under confocal geometry, based on 532 nm laser focused by 100× objective lens (NA = 0.8). The grating was set as 600 g mm⁻¹ (for PL measurement) and 1800 g mm⁻¹ (for Raman measurement).

Numerical Calculations: The full-wave simulations were done by a commercial finite-difference time-domain software (FDTD Solutions, Lumerical Inc) based on normal planewave excitation and periodic boundary conditions in x and y directions. The permittivities of the gold, silicon, and Al₂O₃ were all taken from the software database, with the Johnson-Christy model adopted for the permittivity of gold. The monolayer WS₂ was modelled as a 0.618 nm thick dielectric layer, whose permittivity modelled as Lorentzian oscillator^[64,65] $\epsilon(E) = 1 + \sum_{k=1}^N f_k / (E_k^2 - E^2 - i\gamma_k E)$. Here, f_k and γ_k are the oscillator strength and the linewidth of the k th oscillator and E_k is the oscillation energy that runs over the full spectral range.

Supporting Information

Supporting Information is available from the Wiley Online Library or from the author.

Acknowledgements

L.L. and L.Y.M.T. contributed equally to this work. This work is supported in part by Singapore Ministry of Education under Grant No. RG177/17, 2017-T1-001-239 (RG91/17 (S)), MOE2018-T2-2-189 (S),

MOE2016-T2-2-159, MOE2016-T2-1-128; A*Star AME programmatic grant no. A18A7b0058, A*Star (SERC 1720700038 and SERC A1883c0002); National Research Foundation Competitive Research Program: NRF-CRP18-2017-02, and the Spanish MINECO under contracts MAT2014-53432-CS-5-R and FIS2015-64951-R. *Author contributions:* Y.L., D.H.Z., and Q.J.W. supervised the project. Y.L. and F.J.G.V. conceived the idea, while L.L. and L.Y.M.T. designed the experiments. L.L. characterized the bright-field and dark-field responses of the WS₂-nanoantenna systems and performed the numerical analysis. L.Y.M.T. fabricated the gold bowtie and square dimer antenna arrays with sub-10 nm gaps and performed data analysis. L.L. performed the photoluminescence and Raman scattering measurements of the CVD-grown and mechanically exfoliated WS₂. J.T. performed atomic layer deposition of Al₂O₃, while X.Y. mechanically exfoliated and transferred monolayer WS₂ on the sample. B.Q. fabricated and performed SEM inspection of gold nanoantenna arrays coupled with exfoliated WS₂. L.L. and L.Y.M.T. wrote the manuscript with the inputs from all authors. All authors discussed the results and commented on the manuscript.

Conflict of Interest

The authors declare no conflict of interest.

Keywords

localized surface plasmons, photoluminescence, polariton, strong coupling, WS₂

Received: June 14, 2019

Revised: August 19, 2019

Published online: September 23, 2019

- [1] K. Huang, *Proc. R. Soc. London, Ser. A* **1951**, 208, 352.
- [2] J. J. Hopfield, *Phys. Rev.* **1958**, 112, 1555.
- [3] Y. J. Chen, E. Burstein, D. L. Mills, *Phys. Rev. Lett.* **1975**, 34, 1516.
- [4] Y. Yamamoto, H. Deng, H. Haug, *Bose-Einstein Condensation of Exciton-Polaritons* **2010**.
- [5] H. Deng, H. Haug, Y. Yamamoto, *Rev. Mod. Phys.* **2010**, 82, 1489.
- [6] H. Deng, G. Weihs, C. Santori, J. Bloch, Y. Yamamoto, *Science* **2002**, 298, 199.
- [7] T. Byrnes, N. Y. Kim, Y. Yamamoto, *Nat. Phys.* **2014**, 10, 803.
- [8] L. Dominici, G. Dagvadorj, J. M. Fellows, D. Ballarini, M. De Giorgi, F. M. Marchetti, B. Piccirillo, L. Marrucci, A. Bramati, G. Gigli, M. H. Szymańska, D. Sanvitto, *Sci. Adv.* **2015**, 1, e1500807.
- [9] L. Chang, X. Jiang, S. Hua, C. Yang, J. Wen, L. Jiang, G. Li, G. Wang, M. Xiao, *Nat. Photonics* **2014**, 8, 524.
- [10] R. El-Ganainy, K. G. Makris, M. Khajavikhan, Z. H. Musslimani, S. Rotter, D. N. Christodoulides, *Nat. Phys.* **2018**, 14, 11.
- [11] D. Ballarini, M. De Giorgi, E. Cancellieri, R. Houdre, E. Giacobino, R. Cingolani, A. Bramati, G. Gigli, D. Sanvitto, in *2013 Conf. Lasers Electro-Optics Eur. Int. Quantum Electron. Conf. CLEO/Europe-IQEC 2013* IEEE, Munich, Germany **2013**.
- [12] A. V. Zasedatelev, A. V. Baranikov, D. Urbonas, F. Scafirimuto, U. Scherf, T. Stöferle, R. F. Mahrt, P. G. Lagoudakis, *Nat. Photonics* **2019**, 13, 378.
- [13] T. Gao, P. S. Eldridge, T. C. H. Liew, S. I. Tsintzos, G. Stavrinidis, G. Deligeorgis, Z. Hatzopoulos, P. G. Savvidis, *Phys. Rev. B* **2012**, 85, 235102.
- [14] T. G. Tiecke, J. D. Thompson, N. P. De Leon, L. R. Liu, V. Vuletić, M. D. Lukin, *Nature* **2014**, 508, 241.
- [15] J. McKeever, A. Boca, A. D. Boozer, J. R. Buck, H. J. Kimble, *Nature* **2003**, 425, 268.
- [16] D. G. Baranov, M. Wersäll, J. Cuadra, T. J. Antosiewicz, T. Shegai, *ACS Photonics* **2018**, 5, 24.
- [17] B. Lee, J. Park, G. H. Han, H. S. Ee, C. H. Naylor, W. Liu, A. T. C. Johnson, R. Agarwal, *Nano Lett.* **2015**, 15, 3646.
- [18] K. Børkje, A. Nunnenkamp, J. D. Teufel, S. M. Girvin, *Phys. Rev. Lett.* **2013**, 111, 053603.
- [19] A. S. Mishchenko, N. Nagaosa, *Phys. Rev. Lett.* **2004**, 93, 036402.
- [20] X. Liu, T. Galfsky, Z. Sun, F. Xia, E. C. Lin, Y. H. Lee, S. Kéna-Cohen, V. M. Menon, *Nat. Photonics* **2015**, 9, 30.
- [21] R. F. Ribeiro, L. A. Martínez-Martínez, M. Du, J. Campos-Gonzalez-Angulo, J. Yuen-Zhou, *Chem. Sci.* **2018**, 9, 6325.
- [22] V. A. Shahnazaryan, V. A. Saroka, I. A. Shelykh, W. L. Barnes, M. E. Portnoi, *ACS Photonics* **2019**, 6, 904.
- [23] E. Cohen-Hoshen, G. W. Bryant, I. Pinkas, J. Sperling, I. Bar-Joseph, *Nano Lett.* **2012**, 12, 4260.
- [24] G. Khitrova, A. Scherer, C. Ell, H. M. Gibbs, J. Hendrickson, T. Yoshie, O. B. Shchekin, D. G. Deppe, G. Rupper, *Nature* **2004**, 432, 200.
- [25] A. Laucht, F. Hofbauer, N. Hauke, J. Angele, S. Stobbe, M. Kaniber, G. Böhm, P. Lodahl, M. C. Amann, J. J. Finley, *New J. Phys.* **2009**, 11, 023034.
- [26] I. J. Luxmoore, R. Toro, O. Del Pozo-Zamudio, N. A. Wasley, E. A. Chekhovich, A. M. Sanchez, R. Beanland, A. M. Fox, M. S. Skolnick, H. Y. Liu, A. I. Tartakovskii, *Sci. Rep.* **2013**, 3, 20.
- [27] M. Cai, O. Painter, K. J. Vahala, *Phys. Rev. Lett.* **2000**, 85, 74.
- [28] J. Dintinger, S. Klein, F. Bustos, W. L. Barnes, T. W. Ebbesen, *Phys. Rev. B* **2005**, 71, 035424.
- [29] J. Dintinger, S. Klein, T. W. Ebbesen, *Adv. Mater.* **2006**, 18, 1267.
- [30] Y. Sugawara, T. A. Kelf, J. J. Baumberg, M. E. Abdelsalam, P. N. Bartlett, *Phys. Rev. Lett.* **2006**, 97, 266808.
- [31] G. A. Wurtz, P. R. Evans, W. Hendren, R. Atkinson, W. Dickson, R. J. Pollard, A. V. Zayats, W. Harrison, C. Bower, *Nano Lett.* **2007**, 7, 1297.
- [32] J. Bellessa, C. Symonds, K. Vynck, A. Lemaitre, A. Brioude, L. Beaur, J. C. Plenet, P. Viste, D. Felbacq, E. Cambril, P. Valvin, *Phys. Rev. B* **2009**, 80, 033303.
- [33] I. Pockrand, J. D. Swalen, R. Santo, A. Brillante, M. R. Philpott, *J. Chem. Phys.* **1978**, 69, 4001.
- [34] R. J. Moerland, H. T. Rekola, *Nano Lett.* **2014**, 14, 1721.
- [35] T. K. Hakala, J. J. Toppari, A. Kuzyk, M. Pettersson, H. Tikkanen, H. Kunttu, P. To, *Phys. Rev. Lett.* **2009**, 103, 053602.
- [36] D. E. Gómez, K. C. Vernon, P. Mulvaney, T. J. Davis, *Nano Lett.* **2010**, 10, 274.
- [37] D. E. Gómez, K. C. Vernon, P. Mulvaney, T. J. Davis, *Appl. Phys. Lett.* **2010**, 96, 073108.
- [38] K. F. Mak, J. Shan, *Nat. Photonics* **2016**, 10, 216.
- [39] X. Duan, C. Wang, A. Pan, R. Yu, X. Duan, *Chem. Soc. Rev.* **2015**, 44, 8859.
- [40] M. E. Kleemann, R. Chikkaraddy, E. M. Alexeev, D. Kos, C. Carnegie, W. Deacon, A. C. De Pury, C. Große, B. De Nijs, J. Mertens, A. I. Tartakovskii, J. J. Baumberg, *Nat. Commun.* **2017**, 8, 1296.
- [41] J. Wen, H. Wang, W. Wang, Z. Deng, C. Zhuang, Y. Zhang, F. Liu, J. She, J. Chen, H. Chen, S. Deng, N. Xu, *Nano Lett.* **2017**, 17, 4689.
- [42] S. Lepeshov, M. Wang, A. Krasnok, O. Kotov, T. Zhang, H. Liu, T. Jiang, B. Korgel, M. Terrones, Y. Zheng, A. Alú, *ACS Appl. Mater. Interfaces* **2018**, 10, 16690.
- [43] M. Stührenberg, B. Munkhbat, D. G. Baranov, J. Cuadra, A. B. Yankovich, T. J. Antosiewicz, E. Olsson, T. Shegai, *Nano Lett.* **2018**, 18, 5938.
- [44] M. Geisler, X. Cui, J. Wang, T. Rindzevicius, L. Gammelgaard, B. S. Jessen, P. A. D. Gonçalves, F. Todisco, P. Bøggild, A. Boisen, M. Wubs, N. A. Mortensen, S. Xiao, N. Stenger, *ACS Photonics* **2019**, 6, 994.

- [45] W. Liu, B. Lee, C. H. Naylor, H. S. Ee, J. Park, A. T. C. Johnson, R. Agarwal, *Nano Lett.* **2016**, *16*, 1262.
- [46] Z. Li, Y. Li, T. Han, X. Wang, Y. Yu, B. Tay, Z. Liu, Z. Fang, *ACS Nano* **2017**, *11*, 1165.
- [47] S. Zu, B. Li, Y. Gong, Z. Li, P. M. Ajayan, Z. Fang, *Adv. Opt. Mater.* **2016**, *4*, 1463.
- [48] S. Wang, S. Li, T. Chervy, A. Shalabney, S. Azzini, E. Orgiu, J. A. Hutchison, C. Genet, P. Samorì, T. W. Ebbesen, *Nano Lett.* **2016**, *16*, 4368.
- [49] A. Kinkhabwala, Z. Yu, S. Fan, Y. Avlasevich, K. Müllen, W. E. Moerner, *Nat. Photonics* **2009**, *3*, 654.
- [50] K. Santhosh, O. Bitton, L. Chuntonov, G. Haran, *Nat. Commun.* **2016**, *7*, ncomms11823.
- [51] R. Q. Li, D. Hernández-Pérez, F. J. García-Vidal, A. I. Fernández-Domínguez, *Phys. Rev. Lett.* **2016**, *117*, 107401.
- [52] S. J. D. Phoenix, P. L. Knight, *Phys. Rev. A* **1991**, *44*, 6023.
- [53] B. W. Shore, P. L. Knight, *J. Mod. Opt.* **1993**, *40*, 1195.
- [54] G. Zengin, M. Wersäll, S. Nilsson, T. J. Antosiewicz, M. Käll, T. Shegai, *Phys. Ref. Lett.* **2015**, *114*, 157401.
- [55] R. Liu, Z. K. Zhou, Y. C. Yu, T. Zhang, H. Wang, G. Liu, Y. Wei, H. Chen, X. H. Wang, *Phys. Rev. Lett.* **2017**, *118*, 237401.
- [56] S. R.-K. Rodriguez, *Eur. J. Phys.* **2016**, *37*, 025802.
- [57] Y. Ding, Y. Wang, J. Ni, L. Shi, S. Shi, W. Tang, *Phys. B* **2011**, *406*, 2254.
- [58] H. Zeng, G. Liu, J. Dai, Y. Yan, B. Zhu, R. He, L. Xie, S. Xu, X. Chen, W. Yao, X. Cui, *Sci. Rep.* **2013**, *3*, 1608.
- [59] R. Esteban, J. Aizpurua, G. W. Bryant, *New J. Phys.* **2014**, *16*, 013052.
- [60] B. Lee, J. Park, G. H. Han, H. Ee, C. H. Naylor, W. Liu, A. T. C. Johnson, R. Agarwal, *Nano Lett.* **2015**, *15*, 3646.
- [61] A. Darweesh, S. Bauman, D. Debu, J. Herzog, *Nanomaterials* **2018**, *8*, 809.
- [62] M. Wersä, J. Cuadra, T. J. Antosiewicz, S. Balci, T. Shegai, M. Wersäll, J. Cuadra, T. J. Antosiewicz, S. Balci, T. Shegai, *Nano Lett.* **2017**, *17*, 551.
- [63] X. Liu, T. Galfsky, Z. Sun, F. Xia, E. Lin, Y.-H. Lee, S. Kéna-Cohen, V. M. Menon, *Nat. Photonics* **2015**, *9*, 30.
- [64] Y. Li, A. Chernikov, X. Zhang, A. Rigosi, H. M. Hill, A. M. Van Der Zande, D. A. Chenet, E. Shih, J. Hone, T. F. Heinz, *Phys. Rev. B* **2014**, *90*, 205422.
- [65] A. Laturia, M. L. Van de Put, W. G. Vandenberghe, *npj 2D Mater. Appl.* **2018**, *2*, 6.